Journal of MATERIALS RESEARCH

Article
DOI: 10.1557/jmr.2019.122

Optimization of anti-solvent engineering toward high performance perovskite solar cells

Jian Li[1,b], Ruihan Yang[1,b], Longcheng Que[1,a], Yafei Wang[1], Feng Wang[1], Jiang Wu[2], Shibin Li[1]

[1]State Key Laboratory of Electronic Thin Films and Integrated Devices, and School of Optoelectronic Science and Engineering, University of Electronic Science and Technology of China (UESTC), Chengdu, Sichuan 610054, China
[2]Institute of Fundamental and Frontier Sciences, University of Electronic Science and Technology of China, Chengdu 610054, China; and Department of Electronic and Electrical Engineering, University College London, London WC1E7JE, U.K.
[a)]Address all correspondence to this author. e-mail: quelongcheng@gmail.com
[b)]These authors contributed equally to this work.

Received: 27 December 2018; accepted: 20 March 2019

Anti-solvent treatment assisted crystallization is currently one of the most widely used methods to obtain high-quality perovskite films ascribed to its great operability. However, choosing a proper anti-solvent toward high-quality perovskite film for perovskite solar cells (PSCs) remains elusive. In this study, we qualitatively evaluate the impact of anti-solvent treatment on the grain growth and phase composition of perovskite by X-ray diffraction, scanning electron microscope, Fourier transform infrared spectrometer, and UV-vis absorption measurement, etc. The results demonstrate that the chemical groups in anti-solvents also affect the formation of perovskites, and anti-solvents with a low boiling point and good polarity contribute to the superior efficiency and reproducibility of PSCs. The device prepared using ether as an anti-solvent exhibits the best power conversion efficiency of 18.47%. The results indicate a new path toward selecting an ideal anti-solvent to improve the performance of PSCs.

Introduction

According to the European Joint Research Center, by 2100, the proportion of renewable energy in the total energy demand will be as high as 86%. Among the renewable energy sources, solar energy accounts for more than 60% of the total energy demand [1]. Recently, organic–inorganic halide perovskites have attracted enormous interest as a new photovoltaic material for solar cells. Since perovskite solar cells (PSCs) based on $CH_3NH_3PbI_3$ were first reported with a power conversion efficiency (PCE) of 3.8% in 2009, the current PCE of PSCs has exceeded 22.1% [2, 3, 4]. Besides the high efficiency, low-temperature solution-based fabrication routes provide an abroad prospect for flexible or tandem modules based on nonheat resistant substrates [5, 6, 7]. In order to realize the commercialization of PSCs, enormous efforts have been made to promote the stability of devices and upscaling [8, 9]. The key to improve PCE of PSCs lies in the optimization of the perovskite layer morphology. Optoelectronic properties of perovskite such as light absorption, charge carrier diffusion length, charge transport, and recombination are directly dependent on film morphology [10, 11, 12, 13]. And as a result, various fabrication methods including anti-solvent treatment (A.S.T.), vacuum evaporation, two-step sequential deposition, vapor assisted deposition, additive-assisted deposition, spray, and doctor blade have been developed to obtain high-quality perovskite films [14, 15, 16, 17, 18]. Among these approaches, anti-solvent method is well developed due to the low cost and feasible operation as well as superior PCE of PSCs.

It is well-known that anti-solvent can speed up the heterogenous nucleation via the quick extraction of solvent to leave solute. In this process, anti-solvent works on the perovskite precursor and dissolved solvent (such as DMSO, DMF, and GBL). It is interesting and meaningful to improve the quality of perovskite films via anti-solvent process and solvent engineering [19]. In 2015, Han et al. used DMSO solvent to retard the crystallization of PbI_2 and thus fabricated a compact PbI_2 film. However, due to the volatility of DMSO, the nucleation rate of the mesophase MAI-PbI_2-DMSO is

https://doi.org/10.1557/jmr.2019.122 Published online by Cambridge University Press

© Materials Research Society 2019

different, which leads to an uneven grain size [20]. It was demonstrated that the kinds of solvents and deposition methods seriously affect the nucleation speed during the deposition processes. In 2014, Xiao et al. screened 12 different kinds of solvents for the treatment of spinning $MAPbI_3$ perovskite film [21]. Anti-solvent engineering has proven to be an effective and facile way to tune the nucleation and crystal growth to obtain high-quality films. However, limited study focuses on the dependence of different anti-solvents on nucleation kinetics of perovskite and PCE of PSCs. Understanding the mechanism of different anti-solvent engineering is crucial for well controlling film morphology and improving performance of PSCs. Meanwhile, environmental-friendly anti-solvents (such as ether, isopropanol, and ethanol) are also rarely employed and investigated. Green anti-solvents have a low boiling point and solubility of perovskite precursors. They are very beneficial to protect the environment and reduce atmosphere pollution while polarity of isopropanol and ethanol can be a big issue for fabricating high performance PSCs. Thus, studying the effects of various anti-solvents with different physicochemical properties on perovskite films formation is urgent and meaningful.

In this paper, we employed six kinds of frequently used and low cost anti-solvents including toluene (Tol), chlorobenzene (CB), ether, isopropanol (IPA), ethanol (Eth), and acetone with different physicochemical properties to treat the spinning perovskite films deposited from a mixed DMSO and DMF solution. The results demonstrate that the anti-solvent shows a significant effect on the perovskite crystal growth kinetics due to different boiling points, polarities, as well as chemical groups. PSCs with the best performance prepared by using anti-solvent of ether yield an efficiency of 18.47%. The results reveal the low cost and facile anti-solvent engineering process is a promising approach for the fabrication of efficient PSCs.

Results and discussion

Figure 1(a) illustrates the preparation procedure for perovskite films by different anti-solvents. Perovskite precursor solution was first dripped on the TiO_2-coated FTO glass substrate and then spun at a fixed rotation speed. Due to the evaporation of solvent during spin coating, the excess solution was spun-off and the perovskite precursor solution was gradually concentrated. Each kind of anti-solvent was then dripped onto the surface of the wet film before the precipitation of perovskite during the spin-coating process. The rapid and homogenous crystallization creates a uniform, dense, and pinhole-free high-quality perovskite thin film because of the quick precapitation.

As shown in Fig. 1(b), six kinds of anti-solvents with different polarities and boiling points were employed in our research. The results show that acetone is a strong polar solvent and may dissolve the precursor of perovskite recipe because the

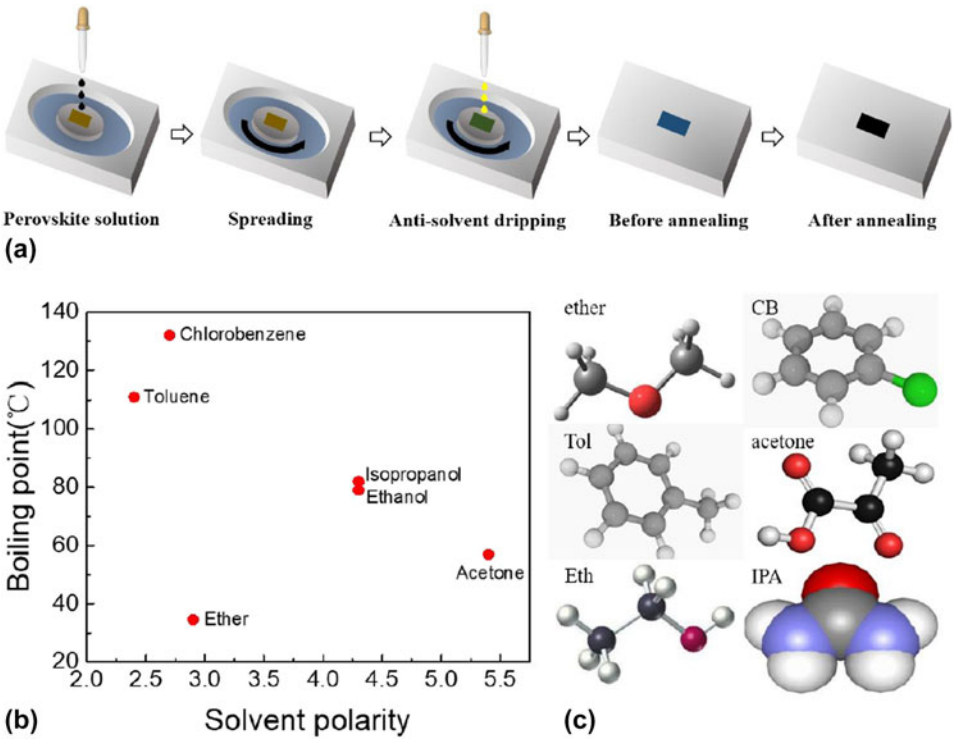


Figure 1: (a) Schematic diagram of anti-solvent assisted perovskite deposition process. (b) Diagraph of boiling point versus polarity of six kinds of anti-solvents. (c) Schematic molecular structures of six kinds of anti-solvents.

https://doi.org/10.1557/jmr.2019.122 Published online by Cambridge University Press

© Materials Research Society 2019

stronger polarity and nonprotic the solution is, the easier the perovskite to dissolve. Therefore, the quality of the film formed by using strong polar solution should be considerably poor. The solvent polarity of Tol, CB, and ether is relatively low to other solvents, which makes those anti-solvents popular for the preparation of perovskite films. Besides, the diagram reveals that CB has the highest boiling point, and solvents with high boiling point dry much slower during the spin-coating, leading to relatively more residual CB solution on perovskite films. Furthermore, CB also does harm to environment and human health. IPA and Eth both have a low boiling point and solubility of perovskite precursors. The polarity of these two anti-solvents is around 4 which is between the polarity of CB and that of acetone. They are very beneficial to protect the environment and reduce atmosphere pollution. In order to explore effect of boiling point and polarity on perovskite formation mechanism, we used these six kinds of solvents with different polarities and boiling points to treat perovskite as anti-solvents on a uniform platform.

As shown in Fig. 2, un-annealed perovskite films exhibit dramatically different textures. The morphology of perovskite films is uneven and poor after treatment by the strong polar solvent acetone because the solvent will dissolve the perovskite films during this process. After treated by ether and Tol anti-solvent, radial needle-shaped crystals grow in the relatively uniform surface. With the treatment of CB, the distribution of needle crystals trends to be more homogenous and denser. There is no thermal contact between the vacuum holder of the spin-coater and the substrate. The evaporative cooling leads to micrometer scale morphology of un-annealed perovskite on the substrate. In this process, nucleation kinetics of anti-solvent method is dominant compared to crystal growth [22]. The needle crystals after ether and CB treatment were more homogenously distributed and denser than those from IPA and Eth treatment. Needle crystals were also obtained through IPA anti-solvent treatment. This should be owed to the quick evaporation of IPA with a low boiling point. After spin-coating, perovskite films with Eth treatment show a low quality surface, which implies an inhomogenous nucleation kinetic. The different colors of each metallographic microscope image thanks to different thicknesses of each film. The size of metallographic microscope image is 6.52 mm length and 4.89 mm width, respectively. Actually, high dissolution of perovskite precursors could result in the rough surface of perovskite films. For the case of CB, ether, and Tol, low polarity around 3 ensures the extraction of perovskite from the high polarity solvent such as DMSO and DMF. The polarity of acetone is about 5.4, which could seriously destroy the formation of perovskite crystals. So, the appropriate polarity of anti-solvent should be between 4.5 and 2.0.

To further study the morphology of the films on a nanometer scale, scanning electron microscope (SEM) images are carried out in Figs. 3(a)–3(e). As shown in Fig. 3(e), it is obviously that the Eth prepared perovskite film exhibits some pinholes. The Eth-treated film shows a large surface inhomogeneity due to the higher polarity and lower boiling point of Eth. According to our previous discussion, polarity and boiling point can seriously affect the nucleation kinetics and the volume of residual anti-solvent. Meanwhile, Eth could decompose the perovskites. Therefore, boundaries and grain size of each $CH_3NH_3PbI_3$ crystal are quite different. IPA washing procedure shows a unique phenomenon here. Grain boundaries of perovskites with IPA washing are not clear and the grain size is larger than that of perovskites with Eth washing. Luckily, perovskite films prepared by IPA washing are very dense. Low solubility of organic components and appropriate polarity are important for the high performance surface morphology of perovskite films. In comparison, perovskite fabricated by CB, ether, and Tol with lower polarities washing shows clear grain boundaries and larger grain size. These

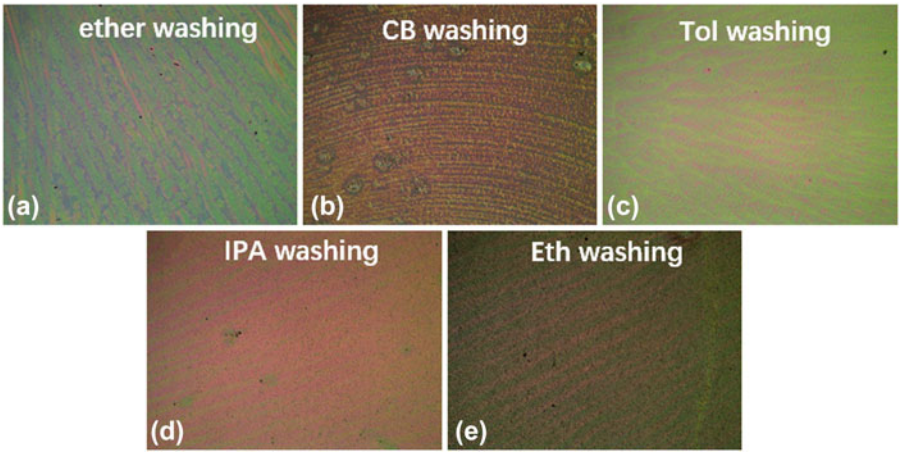


Figure 2: Metallographic microscope images of un-annealed perovskite film treated by anti-solvents (a) ether, (b) CB, (c) Tol, (d) IPA, and (e) Eth.

https://doi.org/10.1557/jmr.2019.122 Published online by Cambridge University Press

© Materials Research Society 2019

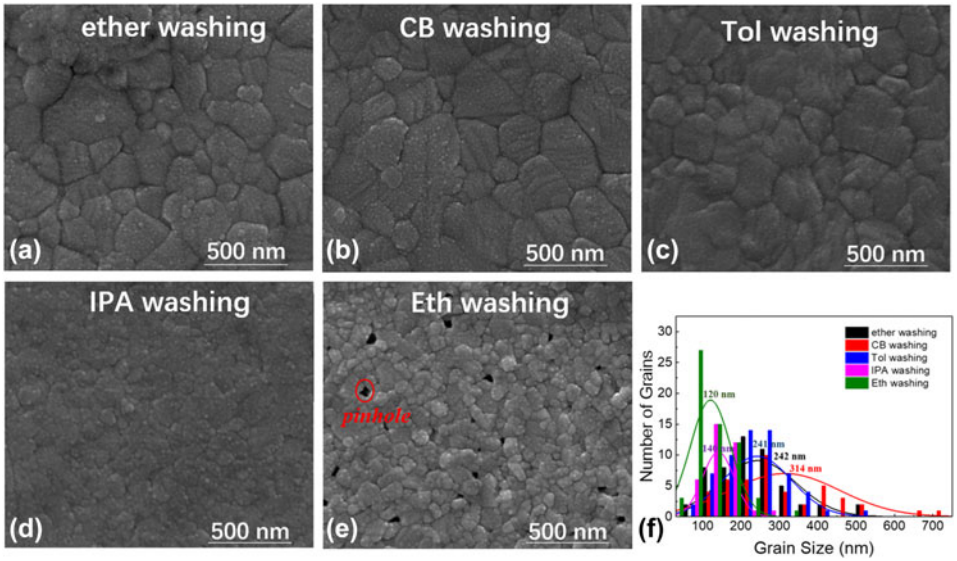


Figure 3: SEM top views of perovskite films treated by (a) ether washing, (b) CB washing, (c) Tol washing, (d) IPA washing, (e) Eth washing, and (f) grain size statistics of perovskite films based on each anti-solvent.

results confirm that the difference in boundaries and grain size of these films attributes to different fabrication processes. The quick separation of perovskite precursors from the solution, the formation of perovskite crystal grains, and the grain boundaries are strongly affected by the polarity and boiling point of the anti-solvent. More nuclei and quicker extraction of perovskite are formed in the washing process with the anti-solvent of low boiling point and low polarity. It is obvious that too fast anti-solvent evaporation leads to a poor extracting of perovskite precursors. As it is shown in Fig. 3, different grain sizes are obtained after treatment by these five anti-solvents. The grain size statistics of perovskite films are also shown in Fig. 3(e) (calculated by Nano Measurement software). The perovskite films treated by ether, CB, and Tol show much bigger perovskite crystals (242, 314, and 241 nm) than the others, which reduce the grain boundaries and the electronic trap states, thus facilitate the charge transport and reduce the recombination [23, 24]. Poor surface morphology of perovskite films treated by IPA and Eth is attributed to relatively high polarity compared to ether, CB, and Tol, which dissolve and decompose little perovskite and perovskite precursor. Meanwhile, we observed that the boiling point is not a key factor for the extraction of perovskite precursors.

Fourier transform infrared spectrometer (FTIR) measurements were carried out to analyze the film forming process after treatment by ether, CB, Tol, IPA, and Eth washing. Here, we studied perovskite films with and without annealing as shown in Figs. 4(a) and 4(b), respectively. The FTIR measurement used transmission mode in the range of 4000–2500 and 1800–800 cm^{-1}. It is obvious that several characteristic peaks related to N–H, C–H, NH_3^+, and C–N which belongs to $CH_3NH_3PbI_3$ are observed in Fig. 4(a). Characteristic frequencies in the IR spectra of perovskite films were shown in Table I. The ν_1 peak at 3185 cm^{-1} is weak for the Eth washing sample compared with this peak of samples with other anti-solvent. This result illustrates Eth could bring away organic cations and is not conductive to form high-quality perovskite. For the case of IPA or ether washing, ν_3, ν_6 – ν_{10}, ν_{12} – ν_{15}, ν_{17} are relatively high. ν_3 is the asymmetric C–H stretching vibration. ν_6 and ν_7 are attributed to vibrational coupled modes which is $\nu_{10/11} + \nu_{13}$. This improvement should be owed to the chemical nature of anti-solvent. ν_8 and ν_9 are asymmetric NH_3^+ bending, ν_{10} is the symmetric NH_3^+ bending, the enhancement of these peaks should be attributed to bending vibrations of NH_3^+. ν_{12} is the asymmetric CH_3 bending mode, ν_{14} and ν_{15} are the CH_3 rocking, and ν_{13}, ν_{17} are the CH_3–NH_3^+ rocking modes. In the formation process of $CH_3NH_3PbI_3$, IPA and ether washing induced the bending vibration of CH_3 and the rocking vibration of CH_3–NH_3^+. We recognized the IPA and ether washing could induce stronger vibration of chemical bonds belonging to $CH_3NH_3PbI_3$ in this anti-solvent. These two solvents contain CH_2 and CH_3 groups, and these chemical groups might react and affect the formation of perovskite crystals. It is interesting that ν_{16} (C–N stretch mode) was weak in IPA processed sample, which indicates there existed different functions between IPA and ether washing. After annealing, a lot of characterized peaks disappeared because of the rearrangement and recrystallization of perovskite crystals. Figure 4(b) (after annealed) shows that only ν_1, ν_2, ν_{10}, ν_{16}, and ν_{17} were observed in the spectrum. As in our previous discussion, ν_1, ν_2, ν_{10}, ν_{16}, and ν_{17} related to N–H stretch, NH_3^+ bending, C–N stretch, and CH_3–NH_3^+ rocking which

https://doi.org/10.1557/jmr.2019.122 Published online by Cambridge University Press

© Materials Research Society 2019

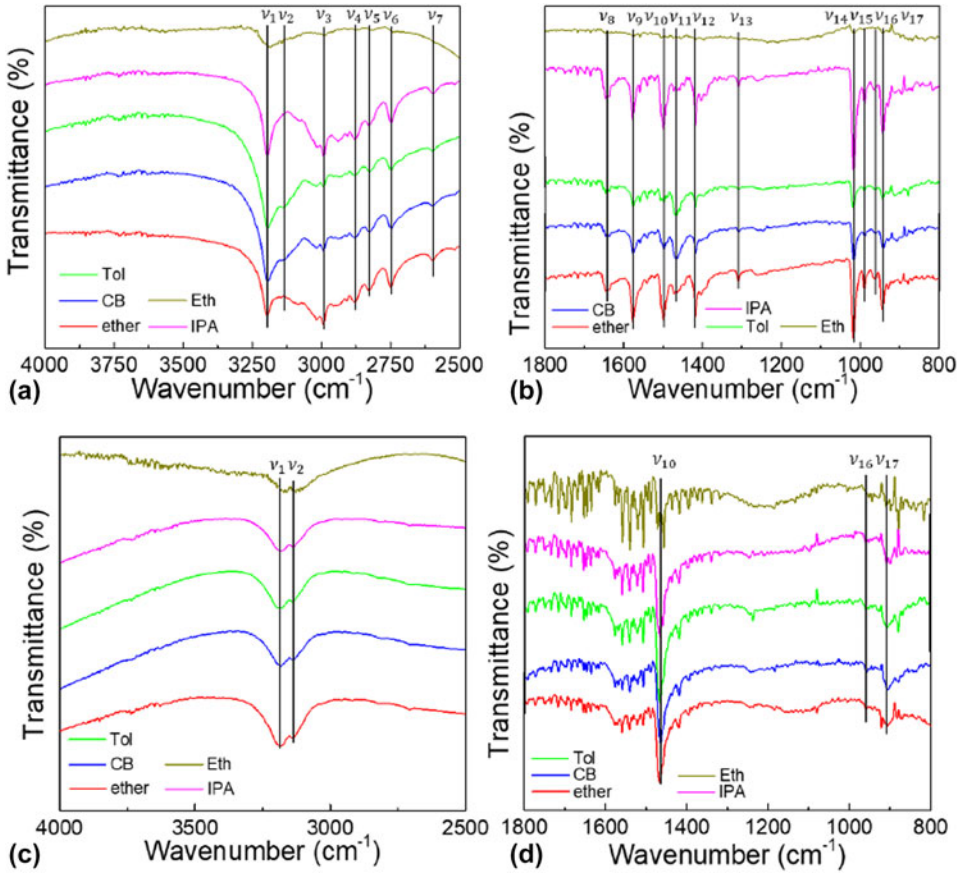


Figure 4: The FTIR of un-annealed perovskite films treated by ether, CB, Tol, IPA, and Eth ranged from (a) 4000–2500 cm^{-1} to (b) 1800–800 cm^{-1}. The FTIR of annealed perovskite films treated by ether, CB, Tol, IPA, and Eth ranged from (c) 4000–2500 cm^{-1} to (d) 1800–800 cm^{-1}.

TABLE I: Characteristic frequencies in the IR spectra of perovskite films.

Vibration	cm^{-1}	Attributed to
ν_1	3185	N–H stretch (asym)
ν_2	3130	N–H stretch (sym)
ν_3	2975	C–H stretch (asym)
ν_4	2885	C–H stretch (sym)
ν_5	2828	$\nu_{8/9} + \nu_{13}$
ν_6	2745	$\nu_{10/11} + \nu_{13}$
ν_7	2600	$\nu_{10/11} + \nu_{13}$
ν_8	1650	NH_3^+ bending (asym)
ν_9	1582	NH_3^+ bending (asym)
ν_{10}	1484	NH_3^+ bending (sym)
ν_{11}	1468	NH_3^+ bending (sym)
ν_{12}	1422	CH_3 bending (asym)
ν_{13}	1315	CH_3–NH_3^+ rocking
ν_{14}	1010	CH_3 rocking
ν_{15}	995	CH_3 rocking
ν_{16}	960	C–N stretch
ν_{17}	950	CH_3–NH_3^+ rocking

could represent the formation of $CH_3NH_3PbI_3$. The high baselines indicate strong light absorption and light scattering.

The UV-visible (range from 400 to 1000 nm) absorption spectra of perovskite films prepared with different anti-solvents were measured and shown in Fig. 5(a). We measured the samples with the films facing to the light. There are similar absorption spectra of perovskite films and based lines except acetone, which should be owed to its strong polarity (polarity = 5.4). Based on our previous discussion, the polarity limit that can dissolve perovskite is more than 4.5. Our results are consistent with the conclusion of Bu et al. [5]. It is also obvious that the absorption of perovskite films obtained via the ether and CB processes is slightly larger at ~760 nm than that of the perovskite films prepared by using other washing solvents. This illustrates the treatment by ether or CB has a great optical absorption of perovskite films. Besides, we intercept UV-Vis absorption spectrum from 700 to 800 nm [Fig. 5(b)] to study this optical absorption in detail. Figure 5(b) shows six absorption steep slopes at 760 nm for perovskite films fabricated by anti-solvent of ether, CB, Tol, IPA, Eth, and acetone, respectively. It is interesting to find that with IPA, perovskite film achieved a relatively high absorption at 760 nm. Meanwhile, the film with Eth washing process exhibits a relatively weak absorption slope at 760 nm, which indicates that the perovskite was not formed well in this process due to the poor solubility of perovskites. However, the baseline of perovskite with IPA or Eth washing is much higher due to the diffuse

https://doi.org/10.1557/jmr.2019.122 Published online by Cambridge University Press

© Materials Research Society 2019

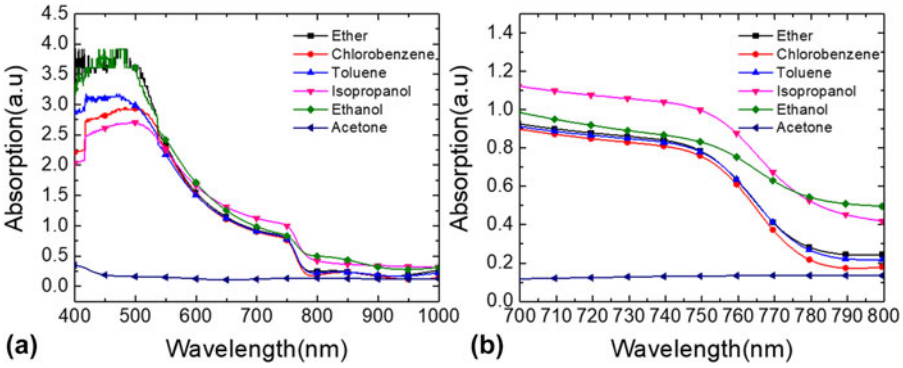


Figure 5: (a) UV-vis absorption spectra of perovskite using different anti-solvents. (b) UV-vis absorption spectra (range from 700 to 800 nm) of perovskite using different anti-solvents.

reflection effect of light. Combined with our previous discussion, IPA or Eth washing leads to a rougher surface of perovskite than that with ether washing. Excessively strong polarity of anti-solvent is really bad for the morphology of perovskite. With ether, CB, and Tol treatment, perovskite films both have a good absorption slope at 760 nm. Therefore, different absorptions of perovskite should be owing to different anti-solvent extraction properties.

X-ray diffraction (XRD) spectra of different anti-solvent engineered perovskite films are shown in Fig. 6(a). The XRD patterns with perovskite peaks are at 14.16° and 28.1°, corresponding to the (110) and (220) planes of $CH_3NH_3PbI_3$, respectively. During thermal treatment, solvent molecules are driven out of the precursors in order to form the final perovskite film. The perovskite peaks of the (110) and (220) are the sharpest and highest for the film prepared by the ether treatment. This suggests that ether can better enhance the crystallinity of $CH_3NH_3PbI_3$ compared to the other anti-solvents. Because of the low boiling point and suitable polarity of ether, there is less residual anti-solvent, which is favorable for the crystallization of perovskite. Perovskite films are fabricated with IPA. CB and Tol washing all have stronger diffraction peaks of the (110) and (220) planes of perovskite, which shows well crystallization of perovskite films in these processes. However, there is an obvious (001) peak of PbI_2 at 12.6° when the IPA washing process was used. This demonstrates that IPA cannot completely extract perovskite precursors during the formation of perovskite crystal. Furthermore, Eth washing process leads to more residual PbI_2, which shows a stronger XRD peak of (001) at 12.6°. Although IPA and Eth are environmental-friendly anti-solvent in fabrication of PSCs, their high polarity has become a big issue. Ether with a suitable boiling point and polarity ensures the best crystallization of perovskite films.

Steady PL measurement results are shown in Fig. 6(b). The perovskite films are deposited on the TiO_2 films. And the film treated by ether has the highest PL intensity. Then the sequence from high to low is Eth, CB, IPA, and Tol. And the PL intensity of IPA and Tol is close. The intensity of steady PL is always associate with nonradiative charge transfer at interface and recombination [25, 26, 27, 28]. This demonstrates the lower nonradiative recombination in the crystal of ether-treated film. According to our device structure, the higher steady PL intensity means there is a lower nonradiative recombination in the crystal of ether-treated film. The treatment by ether results in high-quality perovskite film with lower trap states. Both IPA- and Tol-treated films have very weak steady PL values, which will cause a relatively poor perovskite film performance. It is observed that the PL of perovskite with Eth washing is very high due to the modification of perovskite morphology by Eth washing. This should be owed to the change of the thickness of perovskite films and the increase of diffuse reflection from rough surface. We can see that intensities of integrated steady PL spectra are also consistent with the trend of the V_{OC}, FF, and PCE statistics.

Figure 7(a) presents the current density–voltage (J–V) curves of devices processed in different anti-solvents. The sample fabricated with the ether exhibits the best PCE, which is 18.47%. Such high PCE should be attributed to a lower charge recombination in perovskite film. This result is also consistent with the previous UV-Vis absorption and XRD analysis. The best PCEs under optimized conditions for perovskites with ether, CB, Tol, and IPA are 18.47%, 14.11%, 14.95%, and 8.13%, respectively. Besides, the fill factors of these PSCs based on four kinds of anti-solvents are 71.59, 63.20, 73.46, and 55.44%. The improved performance of the PSC with Ether or toluene is mainly attributed to the increased fill factor. The lower PCE of IPA-treated films can be explained by the SEM images in Fig. 3. We can see that the number of grain boundaries is slightly larger with IPA treatment, which will increase the charge recombination inside the device. The external quantum efficiency (EQE) for the ether-treated solar cell is shown in Fig. 7(b). The perovskite shows a wide photoresponse from 300 to 800 nm, suggesting that solar light can be efficiently collected by the

https://doi.org/10.1557/jmr.2019.122 Published online by Cambridge University Press

© Materials Research Society 2019

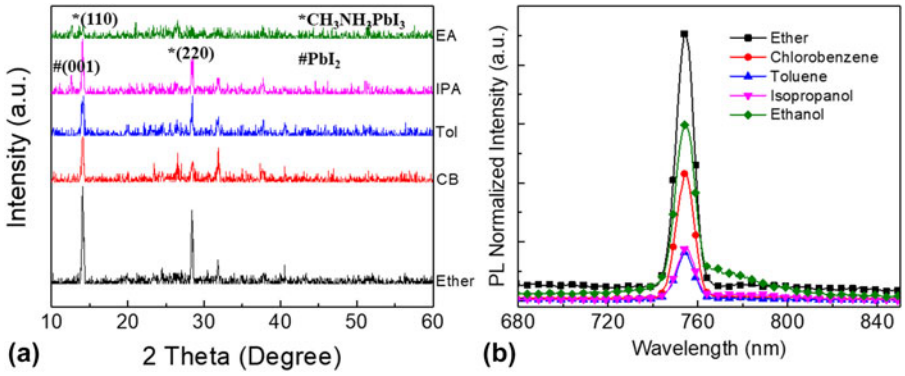


Figure 6: (a) XRD patterns of perovskite films treated with different anti-solvents. (b) Steady-state absorption spectra of perovskite film prepared under different anti-solvent treatments after annealing.

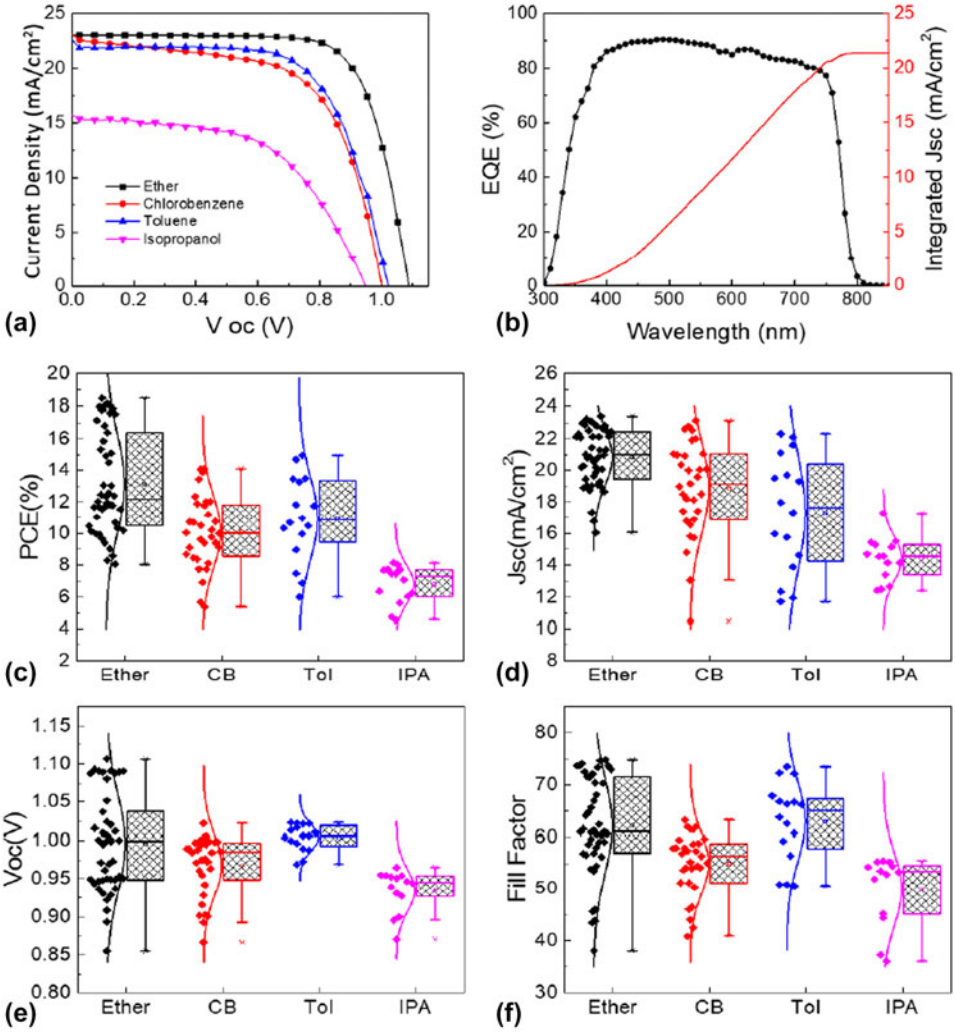


Figure 7: Statistics of parameters obtained from each anti-solvent treatment. (a) *J–V* curves of the solar cell samples with ether, CB, Tol, and IPA. (b) EQE spectra of ether treated PSC. Distribution of the (c) efficiency, (d) J_{SC}, (e) V_{OC}, and (f) FF of the devices with different anti-solvents processes.

terminal electrode and be converted to charge carriers, which results in the high photocurrent density of the PSC. Meanwhile, the estimated J_{SC} value was in good agreement with the J_{SC} values from the *J–V* measurement.

Figures 7(c)–7(f) show parameter (PCE, J_{SC}, V_{OC}, and FF) statistics of devices processed by using different anti-solvents. It is clear that PCE, J_{SC}, V_{OC}, and FF all exhibit a similar trend with the result illustrated in Fig. 4(b). The difference is reflected

https://doi.org/10.1557/jmr.2019.122 Published online by Cambridge University Press

© Materials Research Society 2019

in the contact quality with hole transport layer (HTL) and the morphology of perovskite, which determines the series resistance (R_S) and parallel resistance (R_{SH}) of the total device, respectively. As shown in Fig. 7(d), the sample treated by ether has a relatively high current density (J_{SC}), which illustrates ether treatment can reduce the recombination significantly. It is reported that V_{OC} and FF can reflect the junction properties of PSCs [29]. Higher V_{OC} and FF lead to an improvement of PCE, which are attributed to the enhancement of the quality of perovskite films. We also observe that the distribution of these parameters of PSCs with IPA washing is more concentrated and uniform. This confirms IPA anti-solvent washing has a useful modification for $CH_3NH_3PbI_3$ films.

Conclusion

In this study, we optimized anti-solvent treatment for perovskite film crystallization. The results demonstrate that anti-solvents with both low boiling point and good polarity lead to high-quality PSCs. Besides, some chemical groups (such as CH_2 and CH_3) in anti-solvent (IPA and ether) also induced stronger vibration of chemical bonds and then affected the formation of perovskite. The polarity of anti-solvents plays a crucial role in the solubility of solution (DMF/DMSO). Furthermore, low boiling point creates a suitable environment for perovskite film on the spin substrate to evaporate the mixed anti-solvent and solution solvents (DMF/DMSO) fast and effectively. The PCE of PSCs exhibits a best performance of 18.47% by using ether as an anti-solvent.

Experimental methods

Device fabrication

FTO glass substrates were cleaned sequentially in alkaline detergent, acetone, ethanol, and DI water for 15 min each, followed by drying with N_2 flow. A compact layer of TiO_2 was deposited via spray pyrolysis at 500 °C from a precursor solution of titanium diisopropoxide bis (acetylacetonate) in ethanol (volume ratio, 1:39). The films were annealed at 500 °C for 20 min and then cooled down to room temperature. The mesoporous TiO_2 scaffold was spin-coated at 4000 rpm for 30 s and annealed at 500 °C for 20 min, in which the pristine paste was diluted in ethanol (weight ratio, 1:5). $CH_3NH_3PbI_3$ was synthesized using the one-step spin-coating method and the following experiments except for gold deposition were carried out in a glove box in nitrogen. The perovskite solution contains 691.5 mg PbI_2, 238.5 mg MAI in 0.945 mL DMF, and 0.1065 mL DMSO, and stirred more than 2 h. 80 µL perovskite solution was spin-coated at 4500 rpm for 30 s. The anti-solvent was poured on the samples at the end of 25 s. The samples were annealed at 110 °C for 1 h. The substrates were subsequently covered with a 72.3 mg/mL solution of spiro-OMeTAD in 1 mL chlorobenzene with 28.8 µL of added 4-*tert*-butylpyridine, 17.5 µL of a stock solution of 520 mg/mL lithium bis (trifluoromethylsulphonyl)imide in acetonitrile, and 29 µL of 520 mg/mL tris(2-(1*H*-pyrazol-1-yl)-4-*tert*-butylpyridine) cobalt(III) bis (trifluoromethylsulphonyl) imide in acetonitrile. This solution was spin-coated at 4000 rpm for 30 s. Finally, 80 nm of a gold film was deposited using thermal evaporation.

Measurement and characterization

X-ray diffraction (XRD) diagrams were carried out using a Bede D1 system (Scientech, Shanghai, China) with Cu K_α radiation. Scanning electron microscope (SEM) images were obtained using field emission fitting SEM (FEI-Inspect F50, Holland, Thermo Fisher Scientific, Massachusetts). The UV-vis absorption spectrum was measured by an ultraviolet-visible (UV-vis) spectrophotometer (Schimadzu UV-3101 PC, Shimadzu, Kyoto, Japan). Current–voltage measurements were carried out using Keithley 2400 (Keithley, Austin, Texas) under AM 1.5 G illuminations (1000 W/m^2) from a solar simulator (Newport Oriel Solar 3 A Class AAA, 64,023 A). The AM 1.5 G sun light (100 mW/cm^2) was calibrated using a standard Si-solar cell (Oriel, VLSI standards, Newport Corporation, Wuxi, China). Metallographic microscope images were carried out by MZ5000 (Jiangnan Yongxin, Jiangnan Yongxin, Nanjing, China). Steady PL curves were measured by F-4600 Fluorescence Spectrophotometer (HITACHI, Tokyo, Japan). FTIR iS50R was used to measure our Fourier transform infrared (FTIR) spectroscopies.

Acknowledgments

This work was supported by the National Natural Science Foundation of China under Grant Nos. 61421002, 61574029, 61471085, and 61474015.

References

1. **Joint Research Centre**: Available at: http://eC.europA.eu/jrc/eN. (accessed March 15, 2018).
2. **A. Kojima, K. Teshima, Y. Shirai, and T. Miyasaka**: Organometal halide perovskites as visible-light sensitizers for photovoltaic cells. *J. Am. Chem. Soc.* **131**, 6050–6051 (2009).
3. **W.S. Yang, B.W. Park, E.H. Jung, N.J. Jeon, Y.C. Kim, D.U. Lee, S.S. Shin, J. Seo, E.K. Kim, and J.H. Noh**: Iodide management in formamidinium-lead-halide-based perovskite layers for efficient solar cells. *Science* **356**, 1376–1379 (2017).
4. **D. Zhao, Y. Yu, C. Wang, W. Liao, N. Shrestha, C.R. Grice, A. J. Cimaroli, L. Guan, R.J. Ellingson, K. Zhu, X. Zhao, R-G. Xiong, and Y. Yan**: Low-bandgap mixed tin–lead iodide perovskite absorbers with long carrier lifetimes for all-perovskite tandem solar cells. *Nat. Energy* **2**, 17018 (2017).
5. **T. Bu, L. Wu, X. Liu, X. Yang, P. Zhou, X. Yu, T. Qin, J. Shi, S. Wang, and S. Li**: Synergic interface optimization with green

https://doi.org/10.1557/jmr.2019.122 Published online by Cambridge University Press

© Materials Research Society 2019

solvent engineering in mixed perovskite solar cells. *Adv. Energy Mater.* **7**, 1700576 (2017).

6. **S. Li, P. Zhang, Y. Wang, H. Sarvari, D. Liu, J. Wu, Y. Yang, and Z. Wang**: Interface engineering of high efficiency perovskite solar cells based on ZnO nanorods using atomic layer deposition. *Nano Res.* **10**, 1092–1103 (2017).
7. **P. Zhang, J. Wu, T. Zhang, Y. Wang, D. Liu, H. Chen, L. Ji, C. Liu, W. Ahmad, and Z.D. Chen**: Perovskite solar cells with ZnO electron-transporting materials. *Adv. Mater.* **30**, 1703737 (2018).
8. **M.M. Tavakoli, R. Tavakoli, Z. Nourbakhsh, A. Waleed, U. S. Virk, and Z. Fan**: High efficiency and stable perovskite solar cell using ZnO/rGO QDs as an electron transfer layer. *Adv. Mater. Interfaces* **3**, 1500790 (2016).
9. **D. Bi, P. Gao, R. Scopelliti, E. Oveisi, J. Luo, M. Grätzel, A. Hagfeldt, and M.K. Nazeeruddin**: High-performance perovskite solar cells with enhanced environmental stability based on amphiphile-modified $CH_3NH_3PbI_3$. *Adv. Mater.* **28**, 2910–2915 (2016).
10. **L. Zheng, D. Zhang, Y. Ma, Z. Lu, Z. Chen, S. Wang, L. Xiao, and Q. Gong**: Morphology control of the perovskite films for efficient solar cells. *Dalton Trans.* **44**, 10582–10593 (2015).
11. **Y. Wang, D. Liu, P. Zhang, T. Zhang, W. Ahmad, X. Ying, F. Wang, J. Li, L. Chen, and J. Wu**: Reveal the growth mechanism in perovskite films via weakly coordinating solvent annealing. *Sci. China Mater.* **61**, 1536–1548 (2018).
12. **Y. Wang, T. Zhang, P. Zhang, D. Liu, L. Ji, H. Chen, Z.D. Chen, J. Wu, and S. Li**: Solution processed PCBM-$CH_3NH_3PbI_3$ heterojunction photodetectors with enhanced performance and stability. *Org. Electron.* **57**, 263–268 (2018).
13. **T. Zhang, J. Wu, P. Zhang, A. Waseem, Y. Wang, A. Mahdi, H. Chen, C. Gao, Z.D. Chen, Z. Wu, and S. Li**: High speed and stable solution-processed triple cation perovskite photodetectors. *Adv. Opt. Mater.* **6**, 1701341 (2018).
14. **Z. Xiao, R.A. Kerner, L. Zhao, N.L. Tran, K.M. Lee, T.W. Koh, G.D. Scholes, and B.P. Rand**: Efficient perovskite light-emitting diodes featuring nanometre-sized crystallites. *Nat. Photonics* **11**, 108 (2017).
15. **M. Liu, M.B. Johnston, and H.J. Snaith**: Efficient planar heterojunction perovskite solar cells by vapour deposition. *Nature* **501**, 395 (2013).
16. **Y. Wu, F. Li, C. Han, X. Wang, H. Li, M. Cai, Z. Zhou, T. Noda, and L. Han**: Thermally stable $MAPbI_3$ perovskite solar cells with efficiency of 19.19% and area over 1 cm^2 achieved by additive engineering. *Adv. Mater.* **29**, 1701073 (2017).
17. **J. Burschka, N. Pellet, S.J. Moon, R. Humphrybaker, P. Gao, M. K. Nazeeruddin, and M. Grätzel**: Sequential deposition as a route to high-performance perovskite-sensitized solar cells. *Nature* **499**, 316 (2013).
18. **Y. Liu, Y. Zhang, Z. Yang, D. Yang, X. Ren, L. Pang, and S. F. Liu**: Thinness-and shape-controlled growth for ultrathin single-crystalline perovskite wafers for mass production of superior photoelectronic devices. *Adv. Mater.* **28**, 9204–9209 (2016).
19. **Y. Wang, S. Li, P. Zhang, D. Liu, X. Gu, H. Sarvari, Z. Ye, J. Wu, Z. Wang, and Z.D. Chen**: Solvent annealing of PbI_2 for the high-quality crystallization of perovskite films for solar cells with efficiencies exceeding 18%. *Nanoscale* **8**, 19654–19661 (2016).
20. **Y. Rong, Z. Tang, Y. Zhao, X. Zhong, S. Venkatesan, H. Graham, M. Patton, Y. Jing, A.M. Guloy, and Y. Yao**: Solvent engineering towards controlled grain growth in perovskite planar heterojunction solar cells. *Nanoscale* **7**, 10595–10599 (2015).
21. **X. Manda, H. Fuzhi, H. Wenchao, D. Yasmina, Z. Ye, E. Joanne, G.W. Angus, B. Udo, C. Yi Bing, and S. Leone**: A fast deposition-crystallization procedure for highly efficient lead iodide perovskite thin-film solar cells. *Angew. Chem., Int. Ed.* **53**, 9898–9903 (2014).
22. **S. Paek, P. Schouwink, E.N. Athanasopoulou, K.T. Cho, G. Grancini, Y. Lee, Y. Zhang, F. Stellacci, M.K. Nazeeruddin, and P. Gao**: From Nano- to micrometer scale: The role of antisolvent treatment on high performance perovskite solar cells. *Chem. Mater.* **29**, 3490–3498 (2017).
23. **Y. Wang, J. Wu, P. Zhang, D. Liu, T. Zhang, L. Ji, X. Gu, Z. D. Chen, and S. Li**: Stitching triple cation perovskite by a mixed anti-solvent process for high performance perovskite solar cells. *Nano Energy* **39**, 616–625 (2017).
24. **S.K. Pathak, A. Sepe, A. Sadhanala, F. Deschler, A. Haghighirad, N. Sakai, K.C. Goedel, S.D. Stranks, N. K. Noel, and M. Price**: Atmospheric influence upon crystallization and electronic disorder and its impact on the photo-physical properties of organic–inorganic perovskite solar cells. *ACS Nano* **9**, 2311–2320 (2015).
25. **J. Chen, Y. Xiong, Y. Rong, A. Mei, Y. Sheng, P. Jiang, Y. Hu, X. Li, and H. Han**: Solvent effect on the hole-conductor-free fully printable perovskite solar cells. *Nano Energy* **27**, 130–137 (2016).
26. **Y. Ogomi, A. Morita, S. Tsukamoto, T. Saitho, Q. Shen, T. Toyoda, K. Yoshino, S.S. Pandey, T. Ma, and S. Hayase**: All-solid perovskite solar cells with HOCO–R–$NH_3^+I^-$ anchor-group inserted between porous titania and perovskite. *J. Phys. Chem. C* **118**, 16651–16659 (2014).
27. **L. Zuo, Z. Gu, T. Ye, W. Fu, G. Wu, H. Li, and H. Chen**: Enhanced photovoltaic performance of $CH_3NH_3PbI_3$ perovskite solar cells through interfacial engineering using self-assembling monolayer. *J. Am. Chem. Soc.* **137**, 2674–2679 (2015).
28. **Y.C. Shih, Y.B. Lan, C.S. Li, H.C. Hsieh, L. Wang, C.I. Wu, and K.F. Lin**: Amino-acid-induced preferential orientation of perovskite crystals for enhancing interfacial charge transfer and photovoltaic performance. *Small* **13**, 1604305 (2017).
29. **J. Dong, X. Xu, J. Shi, D. Li, Y. Luo, Q. Meng, and Q. Chen**: Suppressing charge recombination in ZnO-nanorod-based perovskite solar cells with atomic-layer-deposition TiO_2. *Chin. Phys. Lett.* **32**, 078401 (2015).

https://doi.org/10.1557/jmr.2019.122 Published online by Cambridge University Press

© Materials Research Society 2019